Experimental and Theoretical Studies of Hybrid $(C_3N_2H_5)_2SbF_5$ Crystal with the Phase Transition

D. Podsiadła[a,*], M. Drozd[b] and B. Andriyevskyy[c]

[a] *Institute of Experimental Physics, University of Wrocław, M. Born Sq. 9, 50-204 Wrocław, Poland*
[b] *Włodzimierz Trzebiatowski Institute of Low Temperature and Structure Research, Polish Academy of Science, Okólna 2, 50-422 Wrocław, Poland*
[c] *Faculty of Electronics and Computer Sciences, Koszalin University of Technology, Śniadeckich 2, 75-453 Koszalin, Poland*

Received: 30.07.2025 & Accepted: 18.11.2025

Doi: 10.12693/APhysPolA.148.240 *e-mail: dorota.podsiadla@uwr.edu.pl

An organic–inorganic compound $(C_3N_2H_5)_2SbF_5$ — bis(imidazolium)pentafluoroantimanate — was investigated. This crystal undergoes a structural phase transition. The phase transition was studied with the use of the infrared spectra of powdered crystal suspended in Nujol and Fluorolube oil in a wide range of internal vibration of the $(C_3N_2H_5)_2^+$ and SbF_5^{2-} ions (i.e., from 4000 to 400 cm^{-1}) in the temperature range from 183 K (154 K in Fluorolube) to 300 K. The room temperature infrared spectrum in KBr and the Raman spectrum were achieved. The infrared measurement results showed a phase transition at 223 K (upon cooling). Temperature-depended changes of wavenumber, half-width, a center of gravity, and bands intensity were analysed in order to describe the contribution of cationic and anionic dynamics to the phase-transition mechanisms. Density functional theory formalism was applied to theoretical studies of normal vibration wavenumbers. For the optimized structure, harmonic frequencies and infrared intensities with Raman activities were calculated by the hybrid tree-parameter density functional model. Hydrogen bonds for the theoretical moiety were found. The results were compared with the experimental data. Electrostatic charges for the investigated molecules were calculated using the natural bond orbital method and Mulliken methods.

topics: bis(imidazolium)pentafluoroantimanate, infrared (IR) and Raman spectra, phase transitions, density functional theory (DFT) calculations

1. Introduction

The $(C_3N_2H_5)_2SbF_5$ crystal (name read as bis(imidazolium)pentafluoroantimonate(III), often abbreviated as IPFA) belongs to the crystal family with stoichiometry A_2SbX_5, where $A = NH_4^+$ cation or $C_3N_2H_5^+$ cation and X = Cl or F. The crystal family of antimonate crystals has been extensively studied [1–4]. Crystals from this family may have domains and exhibit ferroelastic properties and be characterized by phase transitions, e.g. $(NH_4)_2SbF_5$ crystal [5–7].

It should be added that imidazole, whose ions are part of the IPFA crystal, as well as its derivatives, are used in medicine and pharmacy due to their properties [8–10].

The IPFA crystal is a fairly recent addition to the crystal family. Thermal investigation, X-ray diffraction, dielectric measurements [11], and dielectric dispersion study with determination of cationic dynamics [2] were performed on it. Differential scanning calorimetry (DSC) results showed [11] the phase transition (PT) (as the onsets of the heat flow anomaly) at 220 K during heating and at 216 K during cooling.

In the phase above PT (phase I), the crystal belongs to the P*mmn* space group of the orthorhombic system. There are three kinds of symmetry-unrelated imidazolium cations: A, B, and C [11], which are placed in general positions. The imidazolium cations denoted as A and B reveal four positioned models of disorder. The C cation reveals multi-positioned disorder. The site symmetry m of the SbF_5^{2-} anion is realized in phase I.

In the phase below PT (phase II), the crystal belongs to the monoclinic system, with a space group $P2_1/m$. There are also three kinds of imidazolium ions in the structure, but they are fully ordered. An abrupt diminishing of permittivity at PT temperature was observed [2, 11] as related to imidazolium cations ordering.

IR spectroscopy can detect changes in a sample, including changes in molecular interactions that may occur during a structural phase transition in a crystal. Then the research aimed to describe and understand the vibrational properties of the IPFA-building ions and to explain their contribution to the phase transition.

To optimize the interpretation of experimental results, theoretical calculations using density functional theory (DFT) methods were made. Calculation of the theoretical geometry, the theoretical vibrational infrared (IR) spectrum, and Raman modes were performed with Gaussian program. Additionally, the output files of the program allowed for the enumeration of electrostatic charges. Hence, the highest occupied molecular orbital (HOMO) and the lowest unoccupied molecular orbital (LUMO) energies were calculated.

2. Experimental methods

$(C_3N_2H_5)_2SbF_5$ crystals were obtained at room temperature (RT) by a slow evaporation method from the aqueous solution of stoichiometric quantities of imidazole Sb_2O_3 and excess of hydrofluoric acid. In the second stage, small polycrystals were used as seeds in solution to procure monocrystals.

For IR measurements, samples were prepared as suspensions of powder obtained from single crystals in Nujol and Fluorolube mulls. Temperature-dependent IR spectra were measured with a resolution of 1 cm^{-1} in the range 4000–400 cm^{-1} using a Nicolet Nexus FT-IR spectrometer with KBr windows. A total of 128 scans were made and Fourier transformed (FT) to obtain a single spectrum. Measurements were made at several temperatures, from 300 to 183 K on a cooling run. A thermoregulator, working with a Graseby Specac variable-temperature cell, was used to control the temperature. Each spectrum was assembled at a constant temperature. Ttemperature stability was ± 1 K. A Bruker IFS66 spectrometer was used to record the IR room-temperature spectrum in the 4000–400 cm^{-1} wavenumber range on a pellet. The pellet was made from powdered and compressed IPFA crystal and KBr crystal. Resolution was 1 cm^{-1}.

To record the Raman spectra, we used a spectrometer with a Nd:YAG laser beam that excited the system being studied. The room temperature FT-Raman spectrum was measured in the 3600–80 cm^{-1} range with a resolution of 4 cm^{-1} and 128 scans per a spectrum using a Bruker IFS-88 instrument with FRA-106 Raman attachment.

Multifunctional GALACTIC GRAMS/386 program was used for the spectroscopic data analysis. It is worth noting that the band position obtained in the curve analysis can differ slightly from the experimental band position.

3. Computational details

Due to the composition of the tested crystal, theoretical calculations of phonon vibrations were performed using two methods and different programs. First-principles calculations of the phonon vibrations of $(C_3N_2H_5)_2SbF_5$ crystal were performed using the CASTEP code (Cambridge Serial Total Energy Package) [12] based on the density functional theory (DFT) and the plane-wave basis set. The exchange and correlation effects were treated with the Perdew–Burke–Ernzerhof functional for solids (PBESOL) [13] and the norm-conserving pseudopotentials (*.recpot) were used for the calculations together with the plane-wave cutoff energy of 850 eV. For calculation of the phonon infrared modes in the crystal the density functional perturbation theory method (DFPT) has been applied [14]. The corresponding calculations were performed at the electron eigen-energy convergence tolerance of 5.5×10^{-11} eV using the accurately optimized $(C_3N_2H_5)_2SbF_5$ crystal structure at the monoclinic symmetry $P2_1/m$ (space group no. 11) [11].

The next step of the calculations was the use of the Gaussian program. Calculation of the theoretical geometry, IR and Raman spectra were performed with this program (Gaussian 09, revision A.02 [15]). Structural data from X-ray investigations (CCDC [16, 17] no. 1064111) of crystal were used for the calculations. The coordinates for particular atoms were established from the Crystallographic Information File data. The optimized structure has been calculated by the hybrid tree-parameter density functional (DFT/B3LYP) method. Owing to the presence of the antimony element in the investigated structure, the density Gauss Triple-Zeta with polarization (DGTZVP) [18] basis set has been employed (many of the basis sets are not parametrized for 5 row's elements).

For structure optimization, the harmonic frequencies and the infrared intensities with Raman activities were calculated by the DFT/B3LYP model. The DGTZVP basis set was used. The obtained frequencies of stretching and bending vibrations were scaled by 0.96 [19, 20]. The calculated pseudopotential energy distribution (PPED) for the investigated molecule enabled us to make detailed band assignments in the infrared spectra. To establish the direction of the transition dipole moment for the bands in theoretical spectra, the IOP $(7/33 = 1)$ command was used.

Electrostatic charges, HOMO and LUMO energies were analyzed directly from Gaussian program log files. Graphic interpretation of the mentioned properties was made by the Gaussview program [21]. In the cases of HOMO, LUMO, and electrostatic potentials, graphic illustrations of the isosurface with a value equal to 0.01 were used. The

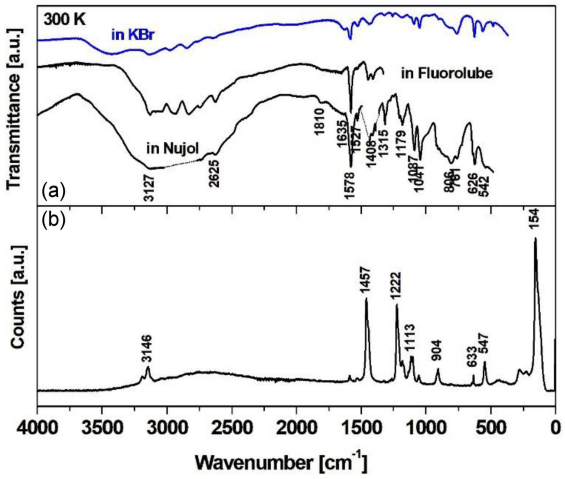

Fig. 1. The experimental spectra of the IPFA crystal at RT (300 K): (a) IR spectra in Nujol and Fluorolube mulls and in KBr pellet, (b) Raman spectrum (proportions are not preserved). The peaks from Nujol have been cut out.

Hirsfeld surface and fingerprint analysis for selected bonds of the investigated crystal were performed using Crystalexplorer program [22].

4. Results and discussion

4.1. Experiments

4.1.1. Experimental IR and Raman spectra

Selected experimental IR spectra in the full spectral range are presented in Fig. 1a. The shown spectra were measured at 300 K in Nujol and Fluorolube oils and in a KBr pellet. Figure 1b also shows the Raman spectrum at RT. Peaks arising due to normal vibrations in Nujol oil are cut out, and the resulting gaps in the spectra are connected by dashed lines. Other spectra measured in Nujol or Fluorolube oils at temperatures below room temperature, up to 193 K, in selected frequency ranges, are presented in the figures later in this paper.

There are two wavenumber ranges in Fig. 1a (in agreement with theory) in which bands exist, i.e., from 3333 cm^{-1} to $\simeq$ 2400 cm^{-1} and below 1600 cm^{-1}. The first range contains bands that appear due to N–H and C–H stretching vibrations, the second due to C–H and N–H bending vibrations, C–C vibrations and Sb–F vibrations. The band at $\simeq$ 3400 cm^{-1} visible in a spectrum measured in the KBr pellet is related to the presence of water in the hygroscopic KBr pellet.

Figure 1b shows the Raman spectrum at RT. Here, we see only one band at wavenumbers above 3000 cm^{-1} (at 3146 cm^{-1}), which is assigned to the ν(C–H) stretching vibrations. In the range below 1500 cm^{-1}, three intensive peaks can be seen

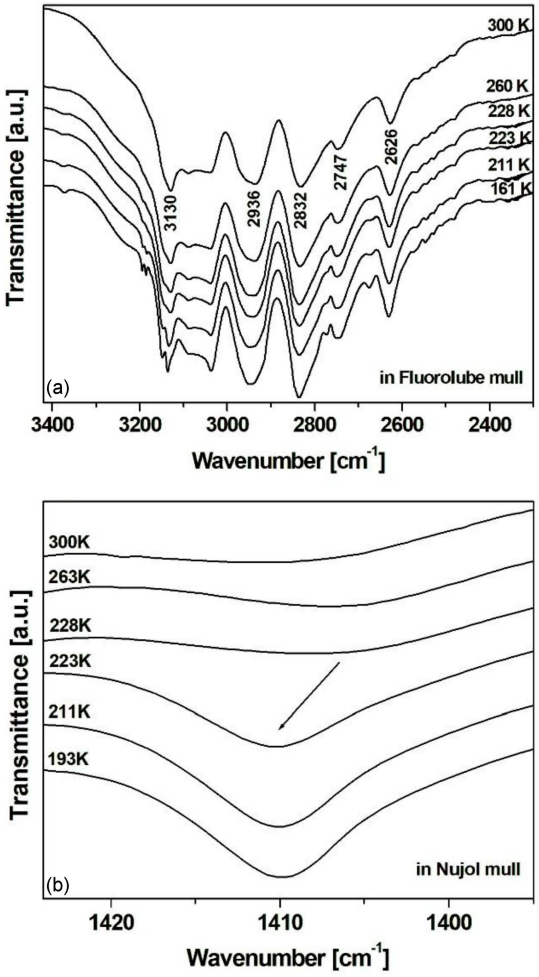

Fig. 2. IR spectra of the IPFA crystal at several temperatures in the range of: (a) N–H and C–H stretching vibrations (3400–2400 cm^{-1}), (b) in-plane bending N–H vibrations (1405–1395 cm^{-1}). The arrow indicates the peak shift.

in Fig. 1b: at 1457, 1222 cm^{-1}, and a very strong one at 154 cm^{-1}. The strongest peak may be related to lattice vibrations (like in [23]). Analogous results were obtained in theoretical calculations, although the intensity is not high there (the results are presented in Table V, Sect. 4.2.2 of in this paper).

The assignments and relative intensities of internal vibrations in the crystal moieties are presented in Table I. Complete assignments of the normal modes of the crystal have been provided by comparison with the IR spectra of imidazole [24, 25], imidazole complexes [26, 27], spectra of tin(II) fluoride compounds [28], antimony compounds [29] and HF–SbF_5 complexes [30]. Data in [31–33] were also considered when identifying the bands in the experimental spectra. The bands for the wavenumbers below 400 cm^{-1} are visible only in the Raman spectrum. They were assigned based on the literature [28, 29, 32] and compared with the results of theoretical calculations (see Table V in Sect. 4.2.2).

TABLE I

Wavenumbers [cm^{-1}], relative intensities, and tentative assignments of the bands observed in the infrared spectra of IPFA crystal at 300 and 219 K for Fluorolube (marked *) and Nujol mulls and Raman spectrum at RT.

IR		Assignment	Raman
300 K	219 K		RT
Band, intensity	Band, intensity		Band, intensity
3147*, sh 3130*, vs	3147*, vs 3135*, vs 3087*, vs, sh	ν(N–H) [25, 26]	3191, vw 3146, w
3036*, vs 2936*, vs 2832*, vs 2747*, s 2626*, m	3038*, vs 2948*, vs 2834*, vs 2749*, s 2630*, m	ν(C–H) [24, 25]	
1579, vs	1576, vs	ν(C–C) [24]	1587, vw
1527, vw	1527, vw	ν(ring) [25]	
1446*, w			
1406*, w	1531*, vw 1410, w	δ(N–H) in plane [31]	1533, vw 1457, s
1315, vw	1311, w 1299, vw	ν(C–N) [24, 25]	
1204, vw, sh 1180, vw	1200, w 1191, w 1171, w	ν(ring)	1222, s 1180, vw
			1132, w
1087, m	1113, w 1090, m 1081, m sh	δ(C–H) in plane [24]	1113, w 1101, vw
1042, m	1047, m 1040, m	δ(C–H) in plane	1053, vw
	991, w		
807, s, br 761, m, sh	917, m 904, m 890, m, sh 880, m 867, m 854, m 812, vs 793, s 773, s 759, m	δ(C–H) out of plane [24, 31] $+\delta$(N–H) out of plane [24] $+\delta$(ring) [24]	904, w 761, m, sh
640, m			
626, s 40, vs, sh	648, m 639, m 627, s 620, s	δ(ring) [24]	633, vw
	561, s	δ(Sb–F) [29, 32]	547, w
			428, vw
		ν(Sb–F) [28, 29, 32] ω(Sb–F) [28, 29, 32] ω(Sb–F) [28, 29, 32]	348, vw, sh 279, vw 224, vw
		lattice vibrations [28]	154, vs

vs — very strong; s — strong; m — medium; w — weak; vw — veryweak; sh — shoulder, br — broad;

The IR transmittance spectra were measured in the spectral range 3400–2400 cm^{-1} for temperatures in the range 161–300 K and are presented in Fig. 2a. The peaks in this wavenumber range have been assigned to the N–H and C–H stretching vibrations, as shown in Table I. It is worth noting that the literature reports various positions of the C–H and N–H stretching bands in this area [24, 25, 27]. We used the results from our theoretical calculations to assign vibrations in this range. It is easy to see that the spectra are quite similar to each other at different temperatures. At first, the peak at 3130 cm^{-1} (at RT) assigned to the ν(N–H) vibrations is almost stable in its position at different temperatures. However, at 211 K, which is below the PT temperature, the peak splits into two components. In higher temperatures, a shoulder appeared in the considered wavenumber range. The changes also are noticeable on the two bottom curves. Similarly, below the PT temperature (i.e., at 223 K), two new peaks appear at 3183 and 3192 cm^{-1}, as seen on the two bottom curves. The remaining peaks in Fig. 2a are assigned to the ν(C–H) vibrations. Some of them — like those at 2936 cm^{-1} and 2747 cm^{-1} — are in stable positions with diminishing temperature, whereas the bands at 2626 cm^{-1} and 2832 cm^{-1} at RT move slightly towards higher wavenumbers with decreasing temperature.

The in-plane bending (N–H) vibrations have been assigned to the peak at about 1406 cm^{-1} (at RT) according to the assignment in [31]. The peaks in the considered spectral range at different temperatures are presented in Fig. 2b. It is easy to see that the nature of the curves at 228 and 223 K (where the phase transition in the crystal occurs) varies dramatically. In Fig. 2b, the band becomes more expressive, increasing in intensity at 223 K and below. The maximum position of the band changes its wavenumber from 1406 cm^{-1} at 300 K to 1410 cm^{-1} at the PT temperature and below. In Fig. 2b it is marked by an arrow. According to Schroetter and Bougeard [34], the shift of the ν(A–H) vibrations to lower frequencies and the δ(A–H) vibrations to higher frequencies is caused by the formation of A–H$\cdots$B complexes. Let's consider the N–H$\cdots$F hydrogen bonds in the IPFA crystal. In [11], all the hydrogen bonds are listed both in phase I (230 K) and phase II (85 K). In phase I, the distances between donors and acceptors, D$\cdots$A, in N–H$\cdots$F hydrogen bonds vary from 2.619(10) Å (for N21–H21$\cdots$F4) to 3.224(8) Å (for N22–H22$\cdots$F1) [11]. In phase II, the bond lengths vary from 2.608(5) Å (for N11–H11$\cdots$F4) [11] to 2.659(5) Å (for N1–H1$\cdots$F4) [11]. (The same bonds, i.e, N11–H11$\cdots$F4 and N1–H1$\cdots$F4 in phase I, have lengths equal to 2.661(13) Å and 3.024(8) Å, respectively.) Thus, according to X-ray data [11], the N–H$\cdots$F hydrogen bonds in IPFA are shortened in phase II (85 K) (they are longer in phase I) and this means that the hydrogen bonds at phase II are stronger. The same can be deducted

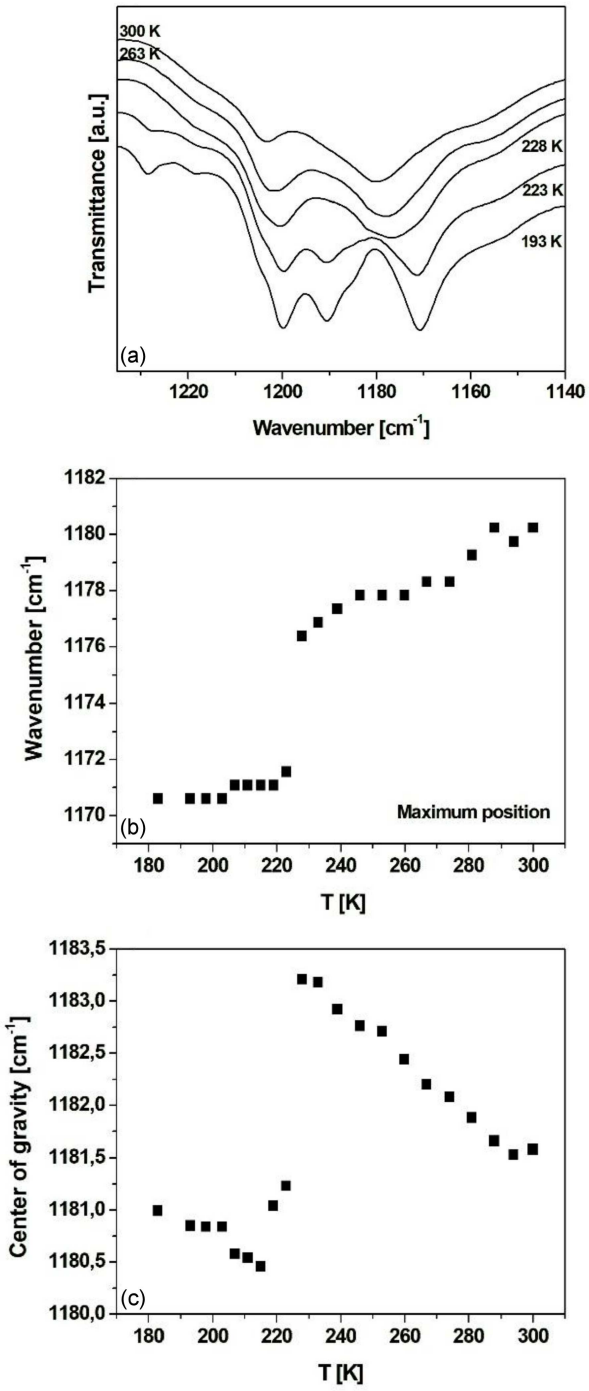

Fig. 3. (a) IR spectra of the IPFA crystal at several temperatures in the range of of ν(ring) vibrations (1140–1235 cm^{-1}). (b) Temperature dependence of the maximum position of the spectral range presented in panel (a). (c) Temperature dependence of the center of gravity for the spectral range shown.

from the IR spectra (Fig. 2a, b). The frequencies of the stretching vibrations ν(N–H) are almost stable with decreasing temperature (Fig. 2a). It is important to note that the band does not move in the

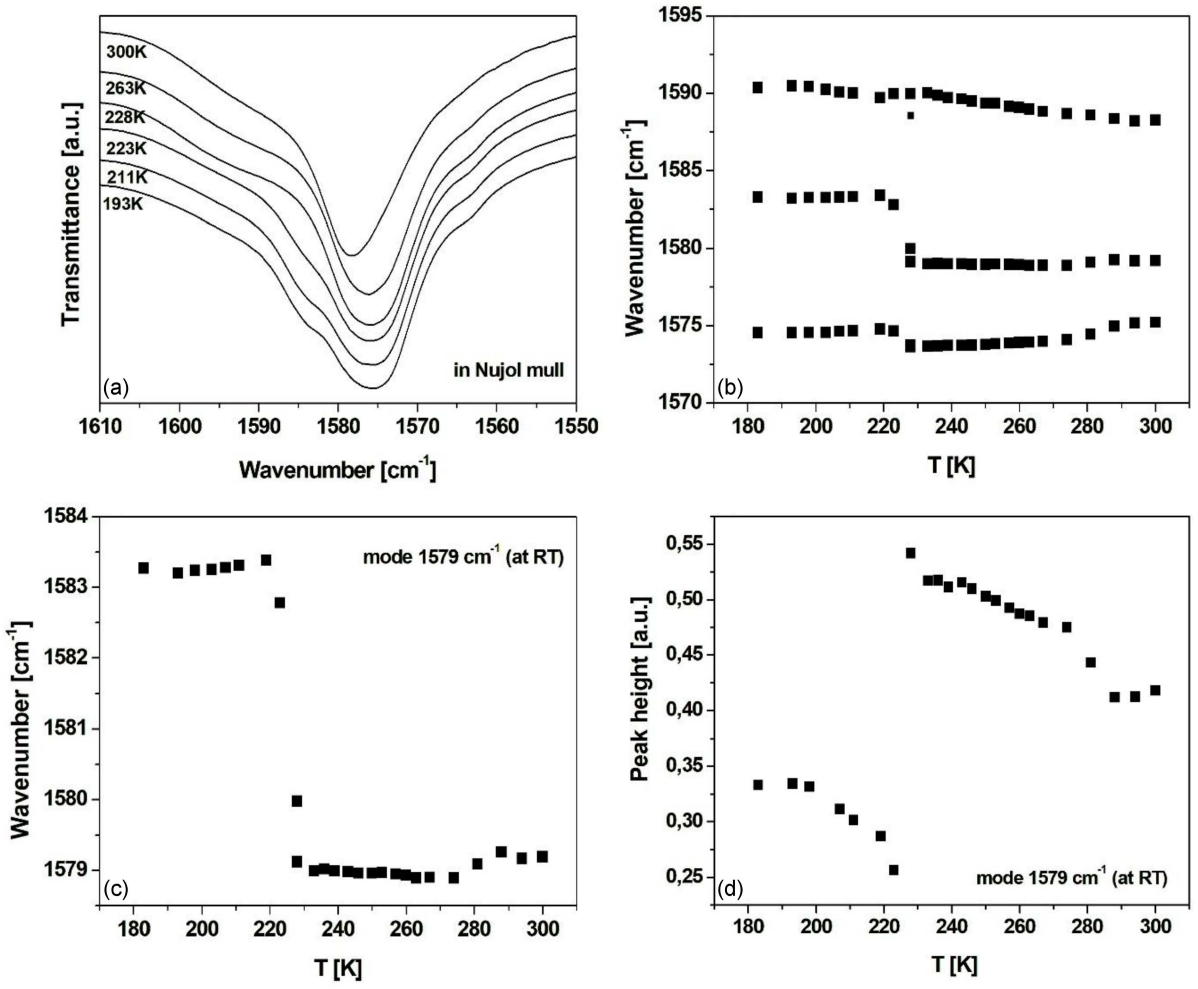

Fig. 4. (a) IR spectra of IPFA crystal in the range of stretching vibrations of C–C groups (1610–1550 cm^{-1}) at different temperatures. (b) Temperature dependence of wavenumbers of peaks fitted in the mentioned range. Evolution of (c) position of the mode at 1579 cm^{-1} and (d) its intensity depending on temperature.

direction of the increasing wavenumber. The δ(N–H) vibrations shift toward higher frequencies together with decreasing temperature (particularly at the PT temperature). Therefore, according to the theory proposed by Schroetter and Bougeard [34], the (N–H) vibrations strengthening is observed in the ordered phase II.

The spectra measured in Nujol mull at different temperatures in the wavenumber range 1140–1235 cm^{-1}, where ν (ring) vibrations occur are shown in Fig. 3a. It is seen that the position of maximum peak moves toward lower wavenumbers during cooling (Fig. 3a, b). Relatively large changes are visible near the PT temperature (Fig. 3a, b). The changes in the spectra (in this case, in peak position) begin at a higher temperature than the PT temperature obtained from DSC measurements. (This could already be seen in Fig. 2b.) IR spectroscopy is more sensitive to the changes in the crystal during the phase transition than DSC methods. Therefore, differences in the phase transition temperature may arise between the results of DSC measurements and measured IR spectra [35]. In Fig. 3a two peaks and two shoulders are visible for the curve at 300 K and above the PT temperature, while five peaks and three shoulders can be distinguished for curves below the PT temperature. Regarding the curve at 193 K (Fig. 3a) there appear the bands at 1171, 1191, 1200, 1218 and, 1224 cm^{-1} and shoulders at 1152 and 1183 cm^{-1}. In phase I (depicted at 300 K in this paper and 230 K in [11]), the crystal structure is disordered. The imidazolium rings occure in a large number of positions, which is described in detail in [11]. However, the spectral peaks in this case are not well resolved. This is precisely what we can observe in Fig. 3a for the transmittance spectra at 300, 263, and 228 K. Below the PT temperature (in phase II, at 85 K in [11]) the crystal is more ordered than in phase I, although cations can still occupy three different positions [11]. In this case, the peaks in the spectra are better resolved, which is visible for curves below the PT temperature, at 223 and 193 K (Fig. 3a).

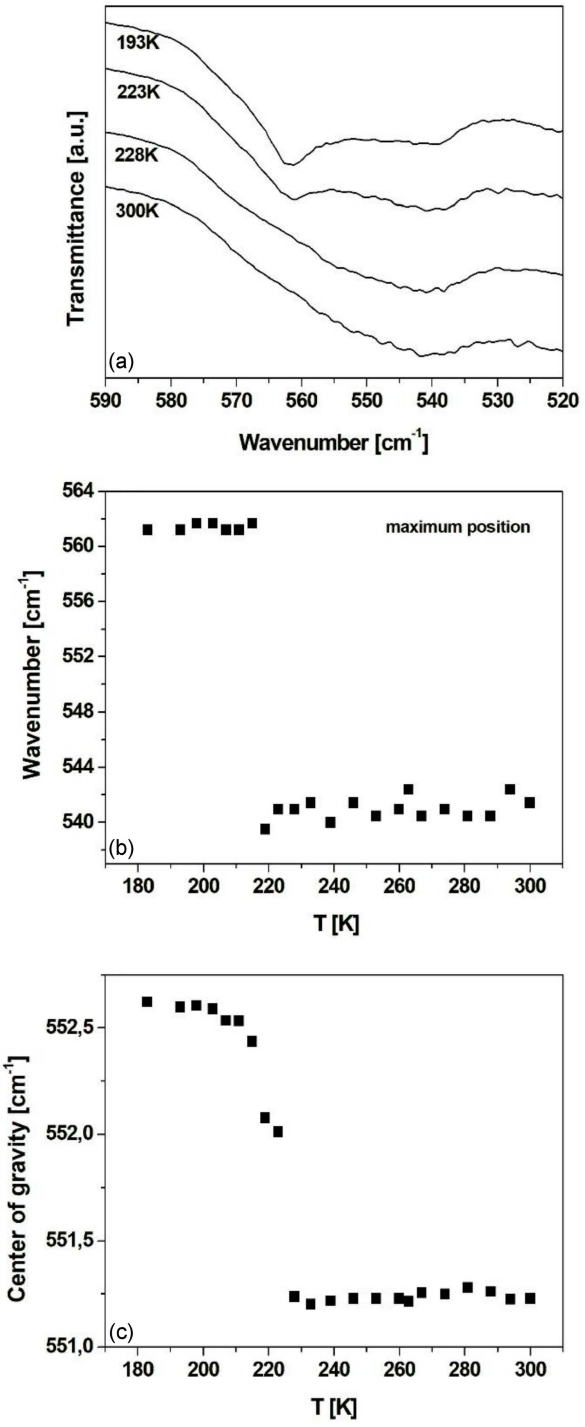

Fig. 5. (a) IR spectra of the IPFA crystal in the range of Sb–F stretching vibrations (590–520 cm^{-1}) at different temperatures. (b) Temperature dependence of the maximum position of the spectral range presented in panel (a). (c) Temperature dependence of the centre of gravity position for the spectral range shown.

Figure 3c presents the temperature changes of the center of gravity position, calculated for the bands presented in Fig. 3a with the use of GRAMS 386 software.

The center of gravity of the band is defined as [36]

$$M^{(1)} = \frac{\int \mathrm{d}\nu\ \nu E_\nu}{\int \mathrm{d}\nu\ E_\nu}\,. \tag{1}$$

It is also called "the first spectral moment" [32] and is applied for asymmetric and complicated contours of absorption bands.

In Fig. 3c, at the PT temparature, the center of gravity position is shifted towards descending values (during a cooling run). The change of position is sharp.

The temperature curves of the IR spectra of the IPFA crystal in the range of stretching vibrations of C–C groups (1610–1550 cm^{-1}) is presented in Fig. 4a. The changes in the spectra are seemingly small. Figure 4b shows the temperature dependence of the wavenumbers of the bands fitted in this spectral range. The experimental asymmetric peak at $\simeq$ 1579 cm^{-1} (at RT) was fitted with two peaks, i.e., one on the position at 1575 cm^{-1} and the second at 1579 cm^{-1}. The two fitted peaks change their positions a few Kelvins above the PT temperature, which is visible in Fig. 4b. Both peak shifts toward higher frequencies (wavenumbers) are small. This indicates that the C–C bonds are shorter. The peak position changes are better seen for the second peak (at 1579 cm^{-1}) and are presented in Fig. 4c, where the abrupt changes occur near the PT temperature.

A baseline was fitted to each measured spectrum. Hence, the peak intensities at different temperatures have the same reference level — the zero level. The changes in the peak intensity for the same mentioned peak near the PT temperature are illustrated in Fig. 4d and are also clear. Figure 4a–d shows that imidazolium cations take part in the phase transition in the IPFA crystal.

Figure 5a presents the normal vibration curves in the frequency range 520–590 cm^{-1} (the range corresponding to the Sb–F vibrations [29, 30, 32]). Although this spectral range is close to the limit of a measuring range, broad peaks are visible. In the cooling run from 300 to 228 K, one peak can be observed at 540 cm^{-1}. This peak is noticeable throughout the range of measured temperatures (to 183 K) at $\simeq$ 540 cm^{-1}. On the curve for 223 K, an additional peak appears at 561 cm^{-1}. The peak is also visible on the other curve in the phase below the PT, i.e., at 193 K. In summary, at temperatures in the vicinity of PT temperature, the new peak — which did not occur at higher temperatures — appears at 561 cm^{-1} (Fig. 5a). Figure 5b shows the temperature dependence of the maximum position in the 520–590 cm^{-1} range. It is clearly visible that in the cooling run from RT to the PT temperature (216 K), the maximum position is almost stable (small differences in the position results from the fact that the band is very broad). At the PT temperature, the maximum position rapidly changes its wavenumber value. At lower temperatures, this position is stable again. The change in the maximum position corresponds very well to the phase

TABLE II

Correlation table for the internal vibrational modes of the IPFA crystal in phase II (at 85 K, $Z = 4$) performed by the correlation method [37, 38].

SbF_5^{2-}			$C_3N_2H_5^+$				
Molecular group C_{4v}	Site group C_1	Factor group C_{2h}	Molecular group C_{2v}	Site group C_1 (C cation)	Factor group C_{2h}	Site group C_s (A, B cations)	Factor group C_{2h}
3 A_1 (IR, R)	12 A	12 A_g (R)	9A_1 (IR, R)	24 A	24 A_g (R)	17A' (IR, R)	17 A_g (R)
B_2 (R)		12 B_g (R)	8B_1 (IR, R)		24 A_u (IR)		17 A_u (IR)
2 B_1 (R)		12 A_u (IR)	3A_2 (R)		24 B_g (R)	7A" (IR, R)	7 B_g (R)
3 E (IR, R)		12 B_u (IR)	4B_2 (IR, R)		24 B_u (IR)		7 B_u (IR)

IR — infrared active; R — Raman-active;

TABLE III

Correlation table for the internal vibrational modes of the IPFA crystal in phase I (at 230 K, $Z = 4$) performed by the correlation method [37, 38].

SbF_5^{2-}			$C_3N_2H_5^+$ (A, B, C cations)		
Molecular group C_{4v}	Site group C_s	Factor group D_{2h}	Molecular group C_{2v}	Site group C_1	Factor group D_{2h}
3 A_1 (IR, R)	8A' (IR,R)	8 Ag (R)	9A_1 (IR, R)	24 A	24 Ag (R)
2 B_1		8 B_1g (R)	3A_2		24 B_1g (R)
3 E (IR)		8 B_2u (IR)	8B_1 (IR)		24 B_2g (R)
		8 B_3u (IR)	4B_2 (IR)		24 B_3g (R)
B_2 (IR)	4A" (IR)	4 B_2g (R)			24 Au
3 E (IR)		4 B_3g (R)			24 B_1u (IR)
		4 Au			24 B_2u (IR)
		4 B_1u (IR)			24 B_3u (IR)

IR — infrared active; R — Raman-active;

transition temperature. In Fig. 5c, the temperature dependence of the center of gravity in the considered wavenumber range is presented. The rapid changes in the center of gravity at the PT temperature quite clearly indicate the existence of a phase transition in the crystal. The temperature dependencies of parameters presented in Fig. 5b, c very clearly illustrate the existence and mechanism of a phase transition in the crystal.

4.1.2. Vibrational study — factor group analysis

The IPFA crystal adopts different space groups in different phases. In phase II (at 85 K according to [11]), IPFA belongs to the space group $P2_1/m$ (C_{2h}^2), a $2/m$ point group of the monoclinic system. The number of molecules in the crystallographic unit cell $Z = 4$ [11] and the number of molecules in the Bravais space cell $Z^B = 4$. Free SbF_5^{2-} anions have C_{4v} symmetry of square pyramid and occupy 12 vibrational modes: $3A_1 + 2B_1 + B_2 + 3E$, as presented in Tables II and III (see also [37, 38]). In phase II, SbF_5^{2-} anion has $C_1(4)$ symmetry in a site group. In a factor group with C_{2h} symmetry for this anion, each of the A vibrational modes redistribute as $A_g + B_g + A_u + B_u$, thus 12 A_u and 12 B_u IR-active and 12 A_g Raman-active modes occur.

The cation $C_3N_2H_5^+$ has C_{2v} symmetry in the free state and occupies 24 normal modes, each of them non-degenerated: $9A_1 + 3A_2 + 8B_1 + 4B_2$. In a site group the imidazolium ions has $C_1(4)$ symmetry (a cation abbreviated as C in [11]) and $C_s(2)$ symmetry (cations abbreviated as A and B in [11]). The C ions occupy 24 A states, and the A and B ions occupy 17 A' and 7 A" vibrational modes, respectively. These modes redistribute in a factor group with C_{2h} symmetry. It is worth remembering that the placement of the cation positions is 0.5 for the C cation, 0.25 for the A cation, and 0.25 for the B cation (from the supplementary information in [11]). The formal classification of the fundamental modes in phase I is shown in Table II.

In phase I, at 230 K (and at RT) the IPFA crystal adopts the space group $Pmmn$ (D_{2h}^{13}); the point group mmm of the orthorhombic system; $Z = 4$ [11]; $Z^B = 4$. This phase shows the disorder

TABLE IV

Comparison between X-ray and theoretical length for selected bonds.

Bond abbreviations	Length experimental [Å]	Length calculated [Å]	Length difference [Å]
Sb–F1	1.942	2.522	0.58
Sb–F2	1.996	2.060	0.064
Sb–F3	1.978	2.060	0.082
Sb–F4	2.259	2.060	−0.199
Sb–F5	2.275	2.060	−0.215
N1–C1	1.318	1.329	0.011
C1–N2	1.321	1.346	0.025
N2–C2	1.373	1.391	0.018
C2–C3	1.345	1.367	0.022
N22–C12	1.320	1.329	0.009
C12–N12	1.320	1.346	0.026
N12–C22	1.371	1.391	0.02
C22–C32	1.360	1.367	0.007
C32–N22	1.371	1.379	0.008

of the imidazolium cations. Both the A, B and C cations has $C_1(8)$ symmetry (general position) in a site group and occupy 24 A modes. (The placement of these positions is 0.5 for the C cation, 0.25 for the A cation, and 0.25 for the B cation). The A vibrational mode redistributes as modes $24A_g + 24B_g + 24A_u + 24B_u$ in a factor group C_{2h}. The anion SbF_5^{2-} occupies the $C_s(4)$ sites and a factor group symmetry D_{2h}. The formal classification of the normal modes in the phase I is shown in Table III.

4.2. Theoretical calculations

4.2.1. Theoretical equilibrium structure

The calculated equilibrium geometry for the investigated molecule is shown in Fig. 6. It is composed of an SbF_5 molecule surrounded in a stoichiometric ratio by two imidazolium molecules, which results from previous crystallographic studies. A comparison of chemical bonds selected by X-ray diffraction [11] and theoretically is presented in Table IV. It should be noticed that based on theoretical calculations of vibrational spectra, a structure with minimum local energy was found (no negative frequencies are noticed).

It is clear that in the case of antimony and fluorine bonds the strength of these interactions should be analyzed very carefully, because the theoretical approach for the element Sb is not performed very often [39]. According to our calculation, the results should be noticed as in good agreement with the experimental X-ray data. Based on the X-ray

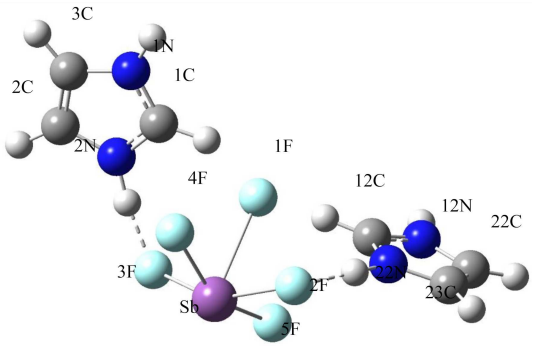

Fig. 6. Theoretical equilibrium geometry of the investigated molecule.

crystallography results, the three Sb–F bonds are very similar and equal to 1.942, 1.996, and 1.978 Å, whereas for the two other Sb–F interactions the experimental bond lengths are longer and equal to 2.259 and 2.275 Å. In the theoretical approach, all Sb–F distances are longer than 2 Å. It should be noticed that three calculated distances are very similar to experimental data and are equal to 2.060 Å. The biggest difference between theoretical and experimental results is noticed for the Sb–F1 interaction. In this case, the theoretical value is equal to 2.522 Å, as presented in Table IV. The significant difference ($\approx$ 0.6 Å) should relate to the calculation method, where hydrogen bonds are not considered (the theoretical calculation used a single-molecule model, as opposed to a structure in which all F atoms engage in hydrogen bonds). The experimental F–Sb–F angles are in the range 79–100°. The shape of the investigated SbF_5^{2-} anion was confirmed by theoretical calculation. The theoretical values of angles are in the range 75–85° and in this case the discrepancies between experimental and calculated values are small.

For C–N bonds, the differences between the experimental and theoretical values are very small. According to the X-ray data, all C–N bonds are included within the short range of 1.318–1.378 Å. It should be noticed that the theoretical data show slightly longer bond lengths, falling within the range 1.329–1.391 Å. In the theoretical approach, all C–N interactions are bigger than experimental. For C–C bonds, the calculated distances are in particularly good agreement with the experimental data. In one case (C2–C3), the calculated distance is slightly longer. For hydrogen atoms in imidazolium rings, the experimental locations were established based on geometrically idealized positions [11]. According to this information, the simple comparison of the C–H and N–H X-ray data with the theoretical results is not possible. All calculated distances mentioned above fall within the range 1.01–1.07 Å. According to the above results, the C–H and N–H bonds lengths established based on the theoretical approach should be recognized as fully realistic.

A more complicated is to compare experimental and theoretical calculations of angles in imidazolium rings. The geometry of the two calculated rings is remarkably similar to the experimental relevance. The rings are flat, practically in both X-ray and theoretical results, for all hydrogens the calculated torsion angles are very close to 180°.

4.2.2. Theoretical spectra

Theoretically calculated wavenumbers for the IR spectra were performed twice with the use of different programs. We wanted to verify whether the different calculations would give comparable results. The results were obtained using the CASTEP code and the optimized $(C_3N_2H_5)_2SbF_5$ crystal structure at the monoclinic symmetry $P2_1/m$ (space group no. 11) [11] is presented in Fig. 7a in the middle. The use of the CASTEP code and a plane-wave basis set was only a prelude to more detailed calculations conducted by the Gaussian program and the density functional triply-parameter hybrid model DFT/B3LYP. In the middle part of Fig. 7a, the peak frequencies are arranged in three groups. The first of them is the small peak group at about 3200 cm^{-1}, the second consist of high intensity single peaks in the wavenumber range 2100–2700 cm^{-1}, and a broad peak group is below 1700 cm^{-1}.

To optimize the first results, the calculations were performed with the use of the Gaussian program and the DFT/B3LYP method, and assuming the equilibrium structure geometry described in Sect. 4.2.1. The theoretical vibrational IR spectrum is shown in Fig. 7a at the bottom, and the theoretical Raman spectrum is shown in Fig. 7b. The results of these calculations will be discussed in detail below. It can be seen in Fig. 7a that the theoretically calculated groups of vibration wavenumbers are close to each other, but not identical. Both calculation codes, i.e, CASTEP and GAUSSIAN, do not accurately predict most of the experimental wavenumbers of the IR absorption spectrum of the $(C_3N_2H_5)_2SbF_5$ crystal in the range of N–H and C–H stretching vibrations. The corresponding calculated results obtained by GAUSSIAN, coincide with the experiment slightly better than those obtained using CASTEP.

Both the theoretical IR and Raman spectra are graphically compared with the experimental spectra, which are also shown in Fig. 1.

Theoretically calculated wavenumbers for the IR and Raman spectra, with the assignments of the observed bands based on potential energy distribution (PED) calculations, are collected in Table V. There are reported 72 vibrations because the GAUSSIAN program gives only frequency and quantities for C1 symmetry of the investigated molecule. The program does not search for additional vibrations if

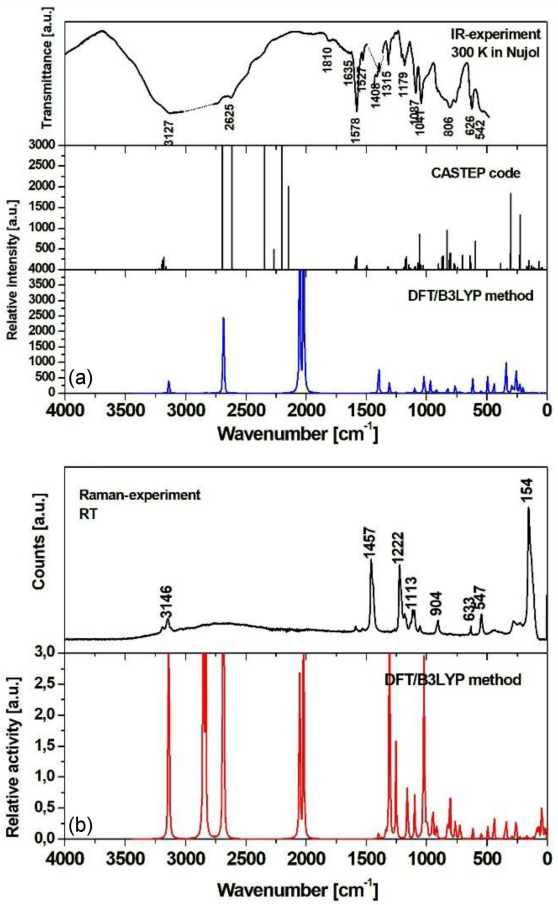

Fig. 7. Comparison of experimental and computational vibrational spectra: (a) IR spectra and (b) Raman spectra. The highest peaks in theoretical spectra are cut for legibility.

they are separated. According to the theoretical approach, the observed bands should be associated with stretching and bending vibrations of: C–H, N–H, C–C, C–N, Sb–F, and hydrogen bonds of N–H···F type.

- N–H vibrations

Based on theoretical calculation, the bands noticed at 3140 and 3139 cm^{-1} were assigned to stretching vibrations of the NH groups. Similar wavenumbers were noticed in other organic compounds with N–H bonds [40, 41]. It should be noticed that the other two very high-intensity bands, originating from this type of vibration, is noticed at 2047 and 2019 cm^{-1}. This is typical because in the PED calculations these vibrations relates to N and H atoms, which are involved in the hydrogen bond network between the two imidazolium rings with the SbF_5 anion. According to the performed calculation, in-plane type of vibrations for the NH groups are noticed in a very wide spectral range. The first region in which these bands are observed is noticed in the range 1398–1158 cm^{-1}. There, 9 bands should be assigned to in-plane (δ) vibrations of the

NH groups. Based on literature data [42, 43], this region should be noticed at ≈ 1500–1600 cm^{-1}. It seems that the single scaling factor used for stretching and bending vibrations in this calculation should be different for both of these vibrations, but since the DGTZVP basis set is used not often, reliable literature data are not available. Interestingly, in mentioned region, i.e., 1398–1158 cm^{-1}), only one band (at 1395 cm^{-1}) was assigned to this type of vibrations. In other cases, the vibrations have complex properties. Bands classified as resulting from the above-mentioned vibration type are also noticed in the range 1023–763 cm^{-1}. However, below 570 cm^{-1}, the bands are noticed due to out-of-plane type of vibrations of the NH groups. These bands were found in a single range 570–494 cm^{-1}. According to the literature data [30], this assignment should be classified as real.

• C–H vibrations

According to the PED analysis, the bands in the range 2852–2684 cm^{-1} were assigned to stretching vibrations of the CH groups. It should be mentioned that the obtained results are in very good agreement with the literature data [41]. This assignment is ambiguous because these vibrations are non-complex. Much more debatable seem to be the case of the IR intensities obtained from theoretical calculation. The bands connected with antisymmetric stretching vibrations should have higher intensities in the IR spectra observed in the case of symmetric stretching vibrations, but in our calculation this relationship seems to be disturbed. In a wide range 1337–763 cm^{-1}, the bands of bending vibrations of in-plane type are observed. It is clear that in the literature data these bands are noticed in a narrower range (1460–1300 cm^{-1}), but partial participation of the in-plane type vibrations in bands below 1000 cm^{-1} is possible. Based on our calculation, the vibrations of out-of-plane type of CH bending vibrations are expected in the range below 725 cm^{-1}. This is consistent with previous literature data [41].

• C–C vibrations

The bands noticed at 1398, 1337, and 1336 cm^{-1} were assigned to stretching vibrations of C–C bonds in imidazolium rings. It should be emphasized that these values are real and in good agreement with literature data [44]. Based on our calculation, the band at 1398 cm^{-1} should be assigned to the antisymmetrical stretching type of C–C vibrations. According to PED calculations, the bands observed at 1337 and 1336 cm^{-1} were assigned to symmetric stretching vibrations of C–C bonds. An explanation of why single bond in the ring is called symmetric or antisymmetric is provided in the Appendix. Additionally, the bands noticed in the narrow range $\simeq$ 825 cm^{-1} were partly assigned due to in-plane bending vibrations of the aforementioned groups. On the other hand, two bands in the spectrum at 546 and 495 cm^{-1} were assigned to out-of-plane bending vibrations of CC groups. Based on literature data, these wavenumbers have real values.

• C–N vibrations

In the literature, the bands connected with C–N stretching vibrations are very well defined [45]. Usually, these bands occurred in the range 1300–1200 cm^{-1} (antisymmetric stretching) and 1200–1000 cm^{-1} for symmetric stretching. In our calculation, the bands are noticed at 1307, 1305, 1253 and 1252 cm^{-1}. These bands should be partially assigned to antisymmetric stretching vibrations of the CN groups. The bands originating from symmetric stretching vibrations are localized at 994 and 916 cm^{-1}. These results seem to be consistent with the literature. Three bands at 806, 764 and 763 cm^{-1} were assigned to in-plane bending vibrations of CN groups. According to the PED calculation, the bands notice at 570, 569 and 495 cm^{-1} were assigned to the out-of-plane type of the C–N bending vibrations. These values are typical and in good agreement with previous papers.

• Sb–F vibrations

Bands resulting from the presence of antimony as a heavier elements are expected at lower wavenumbers. This assumption was confirmed by our theoretical calculation. The bands observed at 443, 352, 333 and 292 cm^{-1} were assigned to stretching antisymmetric and symmetric vibrations of the SbF groups. Characteristically, these vibrations are practically pure (non-complex) in the PED approach. The bands noticed at 281, 264, 227, 201 and 195 cm^{-1} were assigned as originating from bending vibrations of the mentioned groups. The bands at 352, 264 and 227 cm^{-1} are visible in the experimental Raman spectra (as in Fig. 1b and Table I). As in the case of stretching vibrations, these bending vibrations are defined very well in the PED matrix. Below 150 cm^{-1}, bands connected with libration of SbF_5^{2-} are observed, however in this case these vibrations are mixed with librations of imidazolium rings. According to our calculation, the intensities of these bands in the IR and Raman spectra are very small.

• Hydrogen bond vibrations

In the theoretical approach, only three hydrogen bonds of type N–H$\cdots$F were found [46]. Bands due to stretching vibrations are obtained at 2047 and 2019 cm^{-1}. These theoretical bands are the most intense of all calculated spectra. Of course, the theoretical approach (or one theoretical moiety of the investigated compound of the investigated compound) did not reveal the hydrogen bond network existing in the real crystal, and the mentioned and the mentioned above frequencies (i.e., 2047 and 2019 cm^{-1}) cannot be present in the real spectra. At lower wavenumbers, bands derived from in-plane bending-type vibrations are noticed. Based on PED analysis, the bands at 1292 and 1105 cm^{-1} were assigned to this type of vibrations (δ). Additionally, the two bands noticed at 967 and 965 cm^{-1} were

TABLE V

Theoretical calculated wavenumbers, intensities, and assignments of bands.

Calculated wavenumbers [cm^{-1}]	Scaled wavenumbers [cm^{-1}]	IR intensities [km/mol]	Raman activity [a.u.]	Assignments due to PED analysis	Abbreviation according to Table I for experimental results at RT
3272	3140	53	129	νNH	ν(N–H)
3271	3139	163	52	νNH	ν(N–H)
2972	2852	0.17	166	νCH	ν(C–H)
2971	2851	0.82	77	νCH	ν(C–H)
2954	2835	2.93	70	νCH	
2953	2834	3.63	44	νCH	ν(C–H)
2801	2688	439	128	νCH	
2797	2684	521	85	νCH	ν(C–H)
2133	2047	2680	92	νN–H$\cdots$F	
2104	2019	2948	86	νN–H$\cdots$F	
1456	1398	149	4	δNH, νCC	ν(C–C)
1454	1395	239	0.09	δNH	
1393	1337	0.003	2	δNH, δCH, νCC	ν(ring)
1393	1336	1	0.7	δNH, δCH, νCC	δ(N–H) in plane
1362	1307	35	50	δNH, δCH, νCN	δ(C–H)
1360	1305	97	29	δNH, δCH, νCN	ν(C–N)
1306	1253	6	6	δNH, δCH, νCN	ν(C–N)
1305	1252	9	24	δNH, δCH, νCN	ν(C–N), ν(ring)
1207	1158	7	12	δNH, δCH	
1206	1158	10	8	δCH	
1143	1097	28	12	δCH	δ(C–H) in plane
1142	1096	45	1	δCH	δ(C–H) in plane
1066	1023	108	48	δNH	
1060	1017	165	28	δNH	
1037	995	4.9	0.69	δNH, δCH	
1036	994	1	6	δNH, δCH, νCN	
1007	967	55	0.35	γN–H$\cdots$F	
1005	965	79	0.21	γN–H$\cdots$F	
988	948	7.38	7	δCH	
987	947	9.45	6	δCH	δ(C–H) out of plane
955	917	21	3	δCH	δ(C–H) out of plane
954	916	38	3	δNH, δCH, νCN	δ(N–H) out of plane
859	825	44	4	γCH, δCC	δ(ring)
857	822	33	2	γCH	δ(C–H) out of plane
841	807	1	5	δNH, δCH	δ(N–H) out of plane
840	806	0.1	5	δNH, δCH, δCN	δ(ring)
796	764	49	5	δNH, δCH, δCN	δ(ring)
795	763	71	2	δNH, δCH, δCH	δ(ring)
755	725	8	5	γCH	
755	724	14	1	γCH	
644	618	53	2	γCH	δ(ring)
643	617	106	0.2	γCH	δ(ring)
594	570	0.4	0.2	γNH, γCH, γCN	
593	569	3	0.01	γNH, γCH, γCN	
569	546	15	2	γNH, γCH, γCC	
568	545	23	0.3	γNH, γCH, γCH	
516	495	61	2	γNH, γCH, γCN	
514	494	113	1	γNH, γCH	

TABLE V cont.

Calculated wavenumbers [cm^{-1}]	Scaled wavenumbers [cm^{-1}]	IR intensities [km/mol]	Raman activity [a.u.]	Assignments due to PED analysis	Abbreviation according to Table I for experimental results at RT
462	443	116	6	νSbF, γNH	δ(Sb–F)
367	352	32	3	νSbF	ν(Sb–F)
347	333	341	4	νSbF	
304	292	96	1	νSbF	
293	281	28	0.1	ωSbF	
275	264	31	3	ωSbF	ω(Sb–F)
269	258	329	4	ωSbF	
237	227	150	1	ωSbF	ω(Sb–F)
210	201	48	0.03	ωSbF	
203	195	6	1	ωSbF	
174	167	0.62	1	Lrings	
149	143	2.37	0.1	Lrings	
124	119	5	0.03	Lrings	
123	118	7	1	Lrings	
107	102	0.52	0.07	LSbF, Lrings	
105	101	0.22	2	LSbF, Lrings	
87	83	0.52	2	LSbF, Lrings	
86	83	6	0.18	LSbF, Lrings	
76	73	0.38	0.36	LSbF, Lrings	
74	71	0.62	3	LSbF, Lrings	
49	47	7	2	LSbF, Lrings	
46	44	0.7	6	LSbF, Lrings	
40	39	2	2	LSbF, Lrings	
18	17	3	3	LSbF, Lrings	

ν — stretching vibrations; δ — in-plane bending; γ — out-of-plane bending; ω — SbF bending; L — librations

assigned as originating from out-of-plane bending (γ) vibrations of the N–H$\cdots$F bonds. It should be emphasized that the frequencies of bands due to bending vibrations are very well reconstructed in the theoretical spectra.

4.2.3. HOMO and LUMO

The shapes of the highest occupied molecular orbitals (HOMO) and the lowest unoccupied molecular orbitals (LUMO) are shown in Fig. 8. The calculated HOMO energy is equal to -0.21076 a.u., whereas for LUMO orbital this value is -0.02387 a.u. The calculated HOMO–LUMO gap is equal to -0.18686.

The HOMO for the investigated molecule is symmetrical, practically undisturbed, but not fully localized. In our assumptions, the calculated orbital should be constructed from the p-orbitals of antimony, fluorine, nitrogen, and carbon present in the described molecule, as all the above-mentioned elements are in the p block of the periodic system. In the non-disturbed shape, typical symmetrical dumbbells should be observed. This picture in the real molecule confirms our prediction. For the Sb atom, the huge hemispherical symmetrical shape is observed, and above this typical blurred shape of the p-orbitals from both sides of the Sb atom. The observed shapes of the F atoms are symmetrical and only slightly disturbed. Similar behavior is noticed for the N atoms in imidazolium rings. The calculated HOMO shapes for the N atoms are undisturbed, with typical dumbbell-shapped p-orbitals [47] (this is clearly visible in the case of one imidazolium ring). The symmetrical character of shape is observed close to the C atoms. Of course, the HOMO is visible during the hydrogen bond connecting the imidazolium ring with the F atoms.

The calculated LUMO is located mainly on the imidazolium rings. A small contribution of F atoms is also noticed. In the case of the Sb atom, the LUMO are practically absent. The typical dumbbells shapes are noticed on the F atoms. It should be mentioned that these orbitals are non-disturbed

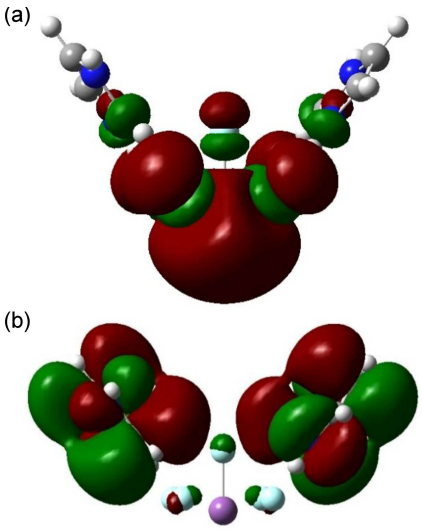

Fig. 8. HOMO (a) and LUMO (b) shapes of an investigated molecule.

without any delocalization. Much more delocalization is observed on the imidazolium rings. In this case, the orbitals of the N and C atoms are not distinguished. Based on performed calculation, the almost full delocalization of the LUMO is shown. A shape of p-orbitals (i.e., dumbbells) is practically not observed. According to these results, the imidazolium rings should be recognized as a more reactive part of the investigated molecule. The formation of a new chemical complex is much more possible through substitution or attachment of new molecules in the imidazolium rings.

4.2.4. Electrostatic charges

The electrostatic charges for investigated molecules were calculated using the natural bond orbital (NBO) method [48] and the Mulliken methods. The results are shown in Fig. 9. It should be mentioned that both calculations give extremely different results. In our opinion, the charges obtained with the NBO method can be considered as more realistic, and these results will be described in detail.

For the Sb atom, the calculated NBO charge is positive and equal to $2.106e$. For the F atoms (F1–F5), the obtained charges are negative and fall in the narrow range from $-0.781e$ to $-0.748e$. These values strongly depend on the chemical surroundings of the fluorine atoms and their chemical role in hydrogen bonds. For the F atoms involved in hydrogen bonds, the charge values are significantly smaller.

The results obtained in the cases of imidazolium rings for nitrogen are expected. In the case of both imidazolium rings the results obtained are identical.

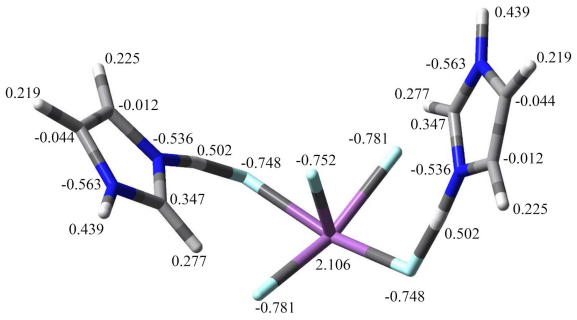

Fig. 9. Calculated NBO charges for the investigated molecule.

The charge of the nitrogen atoms involved in hydrogen bonds is equal to $-0.536e$, whereas for other two N atoms the calculated charge is slightly bigger and equal to $-0.563e$. The obtained results are in good agreement with literature data for similar amino compounds [45, 49].

Surprisingly, the calculated charges for four carbon atoms are negative and range from -0.012 to $-0.044e$, but in the case of two other carbon atoms in the imidazolium ring, positive values of charges are noticed ($0.347e$). These results can be considered typical. In many calculated organic molecules, the mixed charges (positive and negative) are noted for carbon atoms [47].

The calculated values of charges for hydrogen atoms are positive and fall within a wide range $0.219e$–0.225e for hydrogen atoms connected with carbon. A slightly bigger charge value is noticed for protons connected with nitrogen atoms. In this case, the calculated charges are equal to $0.439e$ and $0.502e$ for not-bonding and hydrogen-bonding atoms, respectively. This is typical for organic compounds, and comparable results were obtained for this type of compounds [50].

It should be mentioned that most of the differences in results between the NBO and Mulliken calculation methods were for heavier elements. For example, the charge for the Sb atom calculated using the Mulliken method is equal to $1.389e$. For other atoms (especially C, N, and H) the differences are much smaller.

4.2.5. Simple Hirshfeld surface analysis

In the case of a molecular crystal, where intermolecular interactions are relatively weak compared to intramolecular bonds, analysis of observed weak chemical bonds is crucial. In theoretical chemistry, the Hirshfeld analysis is immensely popular — often used for deep analysis of internuclear distances and angles or studies of molecular packing. The entire concept is based on Desiraju's modern crystal engineering [51].

Hirshfeld's surface (HS) depends on the orientation of the molecule in its neighbourhood, the geometry of the molecule, and the atoms that make close contacts in the chosen molecule. In our opinion, the most important of the crystal structure is the hydrogen bonding interaction of the F···H type.

A plot presented in Fig. 10 can be used to identify patterns associated with specific interactions (in our case, F···H). In the figure, we can observe the distances from the HS to the nearest nucleus outside the surface (or external, de) versus distances from the HS to the nearest nucleus inside the surface (or internal, di). Regarding the use of these quantities, the 2D fingerprint plot appears to be more informative [52].

The standard plot is created by binning the (di, de) pairs in intervals of 0.01 Å and colouring each bin (essentially a pixel) of the resulting 2D histogram as a function of the fraction of surface points in that bin [52].

The H···F contacts contribute ≈ 45% to the overall surface contacts and are the most prominent type of contacts in the IPFA crystal. This agrees with the theoretical approach, where hydrogen bonds of type N-H···F were also found. The F···H interaction forms a pair of spikes in the bottom left corner of Fig. 10, separated along the diagonal. The upper spike is associated with the donor atom, and the lower one is with the acceptor atom.

Widely scattered wings are also visible in the centre of Fig. 10. This type of intermolecular interaction is in agreement with other theoretical possible F···H bindings that have been found in theoretical approach. The range of 2.0–2.4 Å is typical for very weak intermolecular interaction.

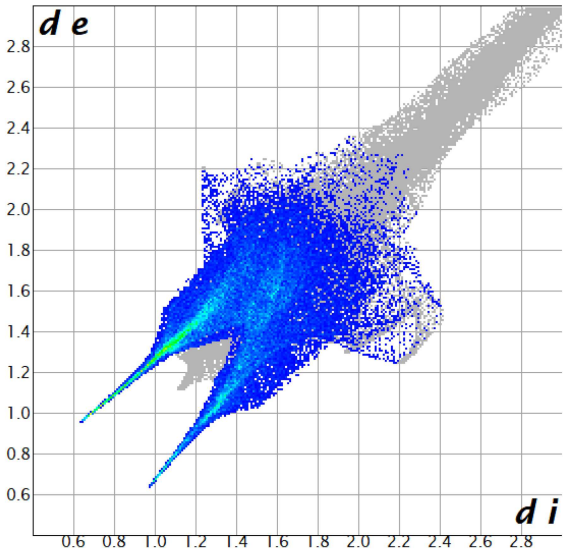

Fig. 10. Fingerprint plot for the investigated single molecule with the contribution of F···H (∼ 45%) interaction.

5. Conclusions

The article presents the results of experimental spectroscopic research and the related extensive theoretical studies. Summarizing what was written in the discussion, it can be stated that:

- The structural phase transition is well reflected in the infrared spectra. Many band parameters change their position or intensity at the phase transition temperature in ways other than just changing these parameters with a temperature change. The changes in the IR spectra indicate the phase transition temperature at 223 K (during cooling).
- The (N–H···F) hydrogen bond strengthening is observed in the ordered phase II.
- The disordering of the imidazolium ring can be concluded based on the spectra.
- Both the cations and anions take part in the phase transition in the IPFA crystal.
- The hydrogen bond lengths of the real and theoretically calculated molecules show fairly good compatibility.
- The assignments of the normal vibration are quite consistent both in theory and experiment, but in the range 2400–1900 cm^{-1} they do not match.
- The theoretical moiety analysis confirmed that the hydrogen bond interaction of the F···H type is the most important in the crystal structure.
- Based on the spectra, it was established that the phase transformation mechanism is mainly related to changes in the imidazole rings.

Acknowledgments

The authors wish to thank Professor Z. Czapla for sample preparation and conception and O. Czupiński PhD for technical assistance in the experiment.

Appendix

Figure 11 illustrate symmetric and antisymmetric vibrations for the C–C bond, according to Gaussview program and the rules included within that software. In this way, the C–C bond, even though it is a single bond, is defined as either symmetric or antisymmetric.

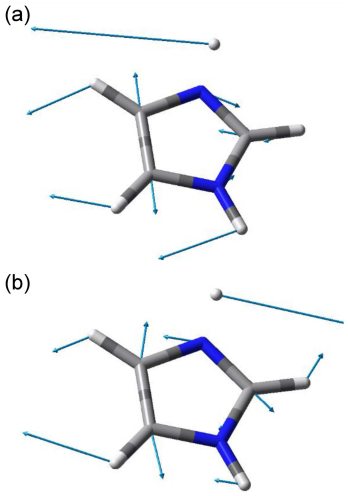

Fig. 11. (a) Symmetrical type of C–C vibrations. (b) Anti-symmetrical type of C–C vibrations.

The arrows illustrate displacement vectors for the C–C bond. In panel (a), they are perfectly parallel and have the same length — a case of symmetric vibrations. In panel (b), they are not parallel — a case of anti-symmetric vibrations.

References

[1] R.R. Ryan, D.T. Cromer, *Inorg. Chem.* **11**, 2322 (1972).

[2] A. Ingram, Z. Czapla, S. Wacke, *Curr. Appl. Phys.* **16**, 278 (2016).

[3] B. Andriyevsky, Z. Czapla, D. Podsiadła, *Mater. Chem. Phys* **205**, 452 (2018).

[4] N. Nakamura, *Z. Naturforsch. A* **41**, 243 (1986).

[5] J. Przesławski, J. Furtak, Z. Czapla, *Ferroelectrics* **337**, 139 (2006).

[6] Z. Czapla, S. Dacko, *Ferroelectrics* **140**, 271 (1993).

[7] B. Andriyevsky, Z. Czapla, V. Stadnyk, *Acta Phys. Pol. A* **87**, 611 (1995).

[8] K. Shalini, P.K. Dharma, N. Kumar, *Der Chemica Sinica* **1**, 36 (2010).

[9] M. Borgers, *Rev. Infect. Dis.* **2**, 520 (1980).

[10] R. Czoik, A. Heintz, E. John, W. Marczak, *Acta Phys. Pol. A* **114**, A-51 (2008).

[11] Z. Czapla, M.K. Krawczyk, A. Ingram, O. Czupiński, *J. Phys. Chem. Sol.* **87**, 233 (2015).

[12] S.J. Clark, M.D. Segall, C.J. Pickard, P.J. Hasnip, M.J. Probert, K. Refson, M.C. Payne, *Z. Kristallogr.* **220**, 567 (2005).

[13] J.P. Perdew, K. Burke, M. Ernzerhof, *Phys. Rev. Lett.* **77**, 3865 (1996).

[14] K. Refson, S.J. Clark, P.R. Tulip, *Phys. Rev. B* **73**, 155114-1 (2006).

[15] M.J. Frisch, G.W. Trucks, H.B. Schlegel et al., Gaussian 09 (now Gaussian 16), Gaussian Inc., Wallingford (CT) 2016.

[16] F.H. Allen, *Acta Crystallogr. Sect. B Struct. Sci.* **58**, 380 (2002).

[17] C.R. Groom, I.J. Bruno, M.P. Lightfoot, S.C. Ward, *Acta Crystallogr. Sect. B Struct. Sci. Cryst. Eng. Mater.* **72**, 171 (2016).

[18] A.G. Yurieva, O.K. Poleshchuk, V.D. Filimonov, *J. Struct. Chem.* **49**, 548 (2008).

[19] K.K. Irikura, R.D. Johnson III, R.N. Kacker, *J. Phys. Chem. A.* **109**, 8430 (2005).

[20] I.M. Alecu, J. Zheng, Y. Zhao, D.G. Truhlar, *J. Chem. Theory Comput.* **6**, 2872 (2010).

[21] R. Dennington, T. Keith, J. Millam, GaussView, Version 5., Semichem Inc., Shawnee Mission (KS) 2009.

[22] D. Jayatilaka, S.K. Wolff, D.J. Grimwood, J.J. McKinnon, M.A. Spackman, *Acta Crystallogr. Sect. A Found. Crystallogr.* **62**, 90 (2006).

[23] J. Baran, Z. Czapla, M.K. Drozd, M.M. Ilczyszyn, M. Marchewka, H. Ratajczak, *J. Mol. Struct.* **403**, 17 (1997).

[24] R. Ramasamy, *Am. J. Phys.* **8**, 51 (2015).

[25] T.J. Lane, I. Nakagawa, J.L. Walter, A.J. Kandathil, *Inorg. Chem.* **1**, 267 (1962).

[26] S.J. Archer, T.P.E. Auf der Heyde, G.A. Foulds, D.A. Thornton, *Transition Met. Chem.* **7**, 59 (1982).

[27] G. Giester, V.V. Ghazaryan, M. Fleck, G.S. Tonoyan, A.M. Petrosyan, *J. Mol. Struct.* **1182**, 317 (2019).

[28] T. Birchall, P.A.W. Dean, R.J. Gillespie, *J. Chem. Soc. A* **1971**, 1778 (1971).

[29] T. Birchall, P.A.W. Dean, B. Della Valle, R.J. Gillespie, *Can. J. Chem.* **51**, 667 (1973).

[30] B. Bonnet, G. Mascherpa, *Inorg. Chem.* **19**, 785 (1980).

[31] R. Infante-Castillo, L.A. Rivera-Montalvo, S.P. Hernández-Rivera, *J. Mol. Struct.* **877**, 10 (2008).

[32] L.E. Alexander, I.R. Beattie, *J. Chem. Soc. A* **1971**, 3092 (1971).

[33] E.R. Talaty, S. Raja, V.J. Storhaug, Andreas Dölle, W.R. Carter, *J. Phys. Chem. B* **108**, 13177 (2004).

[34] S. Schroetter, D. Bougeard, *Ber. Bunsenges. Phys. Chem.* **91**, 1217 (1987).

[35] J. Baran, M. Drozd, T. Lis, H. Ratajczak, *J. Mol. Struct.* **372**, 145 (1995).

[36] V.E. Borisenko, Yu.A. Zavjalova, T.G. Tretjakova, Z.S. Kozlova, A. Koll, *J. Mol. Liq.* **109**, 125 (2004).

[37] W.G. Fateley, F.R. Dollish, N.T. McDevitt, F.F. Bentley, *Infrared and Raman Selection Rules for Molecular and Lattice Vibrations: The Correlation Method*; Wiley-Interscience, A Division of John Wiley & Sons, New York 1972.

[38] Z. Mielke, M. Wierzejewska-Hnat, M. Ilczyszyn, J. Baran, *Ćwiczenia Laboratoryjne z Fizyki Chemicznej*, Wydawnictwo Uniwersytetu Wrocławskiego, Wrocław 1995.

[39] S. DeBeer, F. Neese, in: *Comprehensive Inorganic Chemistry II*, 2nd ed., Elsevier 2013.

[40] M. Drozd, *Spectrochim. Acta A Mol. Biomol. Spectrosc.* **65**, 1069 (2006).

[41] J. Oszust, J. Baran, A. Pietraszko, M. Drozd, *Pol. J. Chem.* **83**, 835 (2009).

[42] M. Drozd, J. Baran, *Spectrochim. Acta A Mol. Biomol. Spectrosc.* **64**, 73 (2006).

[43] M. Trzebiatowska-Gusowska, A. Gągor, J. Baran, M. Drozd, *J. Raman Spectrosc.* **40**, 315 (2009).

[44] N. Sheppard, *Spectrochim. Acta A Mol. Biomol. Spectrosc.* **51**, 1450 (1995).

[45] M. Drozd, D. Dudzic, *Spectrochim. Acta A Mol. Biomol. Spectrosc.* **89**, 243 (2012).

[46] J.A.K. Howard, V.J. Hoy, D. O'Hagan, G.T. Smith, *Tetrahedron* **52**, 12613 (1996).

[47] M. Drozd, M. Daszkiewicz, *J. Mol. Struct.* **1161**, 383 (2018).

[48] E.D. Glendening, C.R. Landis, F. Weinhold, *WIREs Comput. Mol. Sci.* **2**, 1 (2012).

[49] M. Drozd, D. Dudzic, A. Pietraszko, *Spectrochim. Acta A Mol. Biomol. Spectrosc.* **105**, 135 (2013).

[50] M. Drozd, M.K. Marchewka, *J. Mol. Struct. THEOCHEM.* **716**, 175 (2005).

[51] G.R. Desiraju, *Crystal Engineering: The Design of Organic Solids*, Elsevier, Amsterdam 1989.

[52] M.A. Spackman, D. Jayatilaka, *CrystEngComm* **11**, 19 (2009).